



**HAL**  
open science

# PFI-ZEKE photoelectron and high resolution photoionization spectra of ND<sub>3</sub> with MQDT simulations

Tim Softley, F. Merkt, Martin Schaefer, Urs Hollenstein

► **To cite this version:**

Tim Softley, F. Merkt, Martin Schaefer, Urs Hollenstein. PFI-ZEKE photoelectron and high resolution photoionization spectra of ND<sub>3</sub> with MQDT simulations. *Molecular Physics*, 2010, 108 (07-09), pp.1069-1082. 10.1080/00268971003649315 . hal-00596289

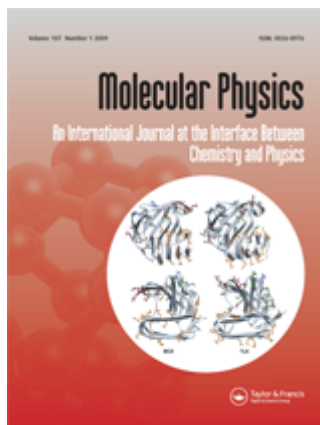
**HAL Id: hal-00596289**

**<https://hal.science/hal-00596289>**

Submitted on 27 May 2011

**HAL** is a multi-disciplinary open access archive for the deposit and dissemination of scientific research documents, whether they are published or not. The documents may come from teaching and research institutions in France or abroad, or from public or private research centers.

L'archive ouverte pluridisciplinaire **HAL**, est destinée au dépôt et à la diffusion de documents scientifiques de niveau recherche, publiés ou non, émanant des établissements d'enseignement et de recherche français ou étrangers, des laboratoires publics ou privés.



## PFI-ZEKE photoelectron and high resolution photoionization spectra of ND<sub>3</sub> with MQDT simulations

Journal:	<i>Molecular Physics</i>
Manuscript ID:	TMPH-2009-0378.R1
Manuscript Type:	Special Issue Paper - In honour of Prof Richard Zare
Date Submitted by the Author:	19-Jan-2010
Complete List of Authors:	Softley, Tim; University of Oxford Merkt, F.; ETH Zurich Schaefer, Martin; ETH Zürich, Laboratorium für Physikalische Chemie Hollenstein, Urs; ETH Zurich
Keywords:	ZEKE spectroscopy, Rydberg spectroscopy, Multichannel quantum defect theory
<p>Note: The following files were submitted by the author for peer review, but cannot be converted to PDF. You must view these files (e.g. movies) online.</p> <p>New WinZip File.zip</p>	



1  
2 **PFI-ZEKE photoelectron and high resolution photoionization spectra of ND<sub>3</sub>**  
3  
4 **with MQDT simulations**  
5  
6  
7

8  
9 L. Duggan<sup>1</sup>, M. Raunhardt<sup>2</sup>, M. Schäfer<sup>2</sup>, U. Hollenstein<sup>2</sup>, T. P. Softley<sup>1</sup>, and  
10  
11 F. Merkt<sup>2</sup>  
12

13  
14 <sup>1</sup>Department of Chemistry, University of Oxford, Chemistry Research Laboratory,  
15  
16 Mansfield Rd, Oxford, OX1 3TA, United Kingdom.  
17

18  
19 <sup>2</sup>Laboratorium für Physikalische Chemie, ETH Zürich, Wolfgang-Pauli-Strasse 10,  
20  
21 CH-8093 Zürich, Switzerland.  
22  
23

24  
25  
26 **Abstract**  
27

28  
29 The rotationally resolved PFI-ZEKE (pulsed-field ionization zero-kinetic energy)  
30  
31 photoelectron spectrum of ND<sub>3</sub> has been recorded at the  $\nu_2^+ = 0, 1$  and 2 thresholds,  
32  
33 by single-photon VUV excitation from the ground-state. An assignment of the  
34  
35  $\tilde{X}^+ \ ^2A_2'' \leftarrow \tilde{X} \ ^1A_1'$  spectrum is presented, allowing a determination of the adiabatic  
36  
37 ionization potential of ND<sub>3</sub> (82261.7(15) cm<sup>-1</sup>) and of the rotational constants and  
38  
39 positions of the  $\nu_2^+ = 0, 1$  and 2 vibrational levels of the ND<sub>3</sub><sup>+</sup> ion. These parameters  
40  
41 are used in a multichannel quantum defect theory (MQDT) simulation of the high-  
42  
43 resolution photoionization spectrum in the range 82100 – 83300 cm<sup>-1</sup> [(R. Seiler *et al.*,  
44  
45 J. Chem. Phys. **118** 10024 (2003)]. A good simulation and an assignment of around  
46  
47 80% of the lines of the ND<sub>3</sub> photoionization spectrum are achieved, verifying the  
48  
49 validity of the molecular constants derived from the PFI-ZEKE photoelectron  
50  
51 spectrum and also the quantum defect parameters derived from *ab initio* calculations.  
52  
53  
54  
55  
56  
57  
58  
59  
60

## (1) Introduction

The ammonia molecule has been, for many years, a model polyatomic system for studies of photoionization dynamics and photoelectron spectroscopy. The photoionization from the ground state is characterized by a large geometry change from pyramidal to planar leading to the characteristic long progression in the out-of-plane (umbrella) bending mode in the photoelectron spectrum [1]. The photoelectron spectrum of  $\text{NH}_3$  has been studied with rotational resolution using pulsed-field ionization zero-kinetic-energy (PFI-ZEKE) photoelectron spectroscopy, both with VUV excitation from the ground state [2 - 4], and using  $(2 + 1')$  resonance-enhanced excitation via the  $\tilde{B}$  state [5]. A mass-analyzed threshold ionization (MATI) spectrum was obtained via the  $\tilde{B}$  and  $\tilde{C}$  states [6,7]. There have also been numerous resonance-enhanced multiphoton ionization (REMPI) studies of the Rydberg states [8 - 14] including some double-resonant studies of higher Rydberg states, and very recently a rotationally resolved study of photoelectron angular distributions has been reported [15].

Very high resolution photoionization spectra of four isotopomers of ammonia  $\text{NH}_3$ ,  $\text{NH}_2\text{D}$ ,  $\text{NHD}_2$  and  $\text{ND}_3$ , were reported by Seiler et al [2]. In comparison with previous studies of the photoionization and photoelectron spectra of  $\text{NH}_3$ , these spectra, recorded using a VUV laser source of bandwidth  $0.008 \text{ cm}^{-1}$ , contain very detailed information on the interactions between the various Rydberg series, and between Rydberg series and continua (including dissociation continua). To assist in the interpretation of these spectra, an *ab-initio* R-matrix calculation of quantum defect parameters for ammonia has been carried out, including the calculation of the geometry dependence of the quantum defects in the  $\nu_2$ -umbrella-bending coordinate, and these parameters have been used to perform multichannel quantum defect theory (MQDT) simulations of the high-resolution photoionization spectrum of  $\text{NH}_3$  [16]. To

1  
2 further test the validity of these quantum defect parameters and the MQDT formalism  
3  
4 used for calculating the spectra [6, 7, 16], it is desirable to extend the MQDT  
5  
6 calculations to the other isotopomers, ND<sub>3</sub>, NH<sub>2</sub>D, and ND<sub>2</sub>H, for which high-  
7  
8 resolution photoionization and photoelectron spectra were also reported in [2,17].  
9  
10 Isotopic substitution does not change the electronic structure and therefore the same  
11  
12 quantum defect matrix should be suitable for the simulation of all isotopomers.  
13  
14 However, isotopic substitution does change the ionization potential, the nuclear spin  
15  
16 statistics, and the rotational constants and vibrational frequencies of the neutral  
17  
18 species and the molecular ion. These differences will not only change the ro-  
19  
20 vibrational limits of each Rydberg series, but also the interactions between the  
21  
22 Rydberg series, having strong effects on the line positions, spectral intensities and  
23  
24 autoionization linewidths.  
25  
26  
27  
28  
29  
30

31 In recent work we reported an assignment of the PFI-ZEKE photoelectron  
32  
33 spectra of the  $v_2^+ = 3$  bands of NH<sub>2</sub>D and NDH<sub>2</sub> and were able to use the information  
34  
35 on rovibrational thresholds derived from these spectra to identify several Rydberg  
36  
37 series in the photoionization spectra [17]. The ND<sub>3</sub> photoionization spectrum reported  
38  
39 in [2] has not been assigned to date, the main difficulty being the uncertainty in the  
40  
41 ionization potential of ND<sub>3</sub>; the best value reported previously was  $82280 \pm 40 \text{ cm}^{-1}$   
42  
43 [8]. The rotational constants for the ND<sub>3</sub><sup>+</sup> ion are also known to much lower precision  
44  
45 than those of NH<sub>3</sub><sup>+</sup> [18], and therefore the identification of the rovibrational Rydberg  
46  
47 series limits in the photoionization spectrum of ND<sub>3</sub> is challenging.  
48  
49  
50  
51  
52

53 In the present paper we report new experimental PFI-ZEKE photoelectron  
54  
55 spectra of ND<sub>3</sub> which allow an accurate determination of the ionization potential, as  
56  
57 well as the spectroscopic parameters of the ion. The accurate energies of the various  
58  
59 ionization thresholds for specific vibration-rotation levels of the ion could then be  
60

1  
2 used, together with *ab initio* quantum defect parameters, to simulate and assign the  
3  
4 photoionization spectrum of ND<sub>3</sub> using MQDT.  
5  
6  
7

## 10 (2) PFI-ZEKE photoelectron spectra of ND<sub>3</sub>

### 12 (2.1) Experimental

13  
14 The PFI-ZEKE photoelectron spectra of ND<sub>3</sub><sup>+</sup> in the region of the  $v_2^+ = 0$ ,  $v_2^+ = 1$  and  
15  
16  $v_2^+ = 2$  ionization thresholds were recorded using an experimental apparatus similar to  
17  
18 that described in Ref. [19]. In brief, the spectra were recorded following single-photon  
19  
20 VUV excitation from the lowest rotation-inversion levels of the ground neutral state  
21  
22 in a skimmed pulsed molecular beam of ND<sub>3</sub> gas. Tunable VUV radiation in the  
23  
24 wavenumber range 82000 - 85000 cm<sup>-1</sup> was produced by resonance-enhanced  
25  
26 difference-frequency mixing  $\nu_{\text{VUV}} = 2\nu_1 - \nu_2$  in a krypton gas jet using the  $(4p)^5 \ ^2P_{1/2}$   
27  
28  $5p' \ [1/2] \ (J = 0) \leftarrow (4p)^6 \ ^1S_0$  two-photon resonance at  $2\tilde{\nu}_1 = 98855.071\text{cm}^{-1}$ . The  
29  
30 tunability of the VUV radiation was achieved by scanning the frequency  $\nu_2$ . The  
31  
32 fundamental frequencies  $\nu_1$  and  $\nu_2$  were generated from the output of two pulsed dye  
33  
34 lasers (Lambda Physik, Scanmate 2e), the first one being frequency tripled. The  
35  
36 resultant VUV radiation had a bandwidth of about 0.4 cm<sup>-1</sup>. The ND<sub>3</sub> gas sample  
37  
38 was diluted in a 1:4 mixture with argon and introduced into the spectrometer via a  
39  
40 pulsed supersonic expansion. This expansion was crossed by the VUV radiation beam  
41  
42 at right angles in the middle of a set of six cylindrical electrodes used to apply the  
43  
44 pulsed electric fields.  
45  
46  
47  
48  
49  
50  
51  
52

53  
54  
55 PFI-ZEKE photoelectron spectra were recorded by monitoring the wavenumber-  
56  
57 dependent electron signal produced by delayed pulsed-field ionization of very high  
58  
59 Rydberg states located below the successive ionization thresholds. A two-pulse  
60  
electric field sequence was employed for field ionization in order to improve the

1  
2 spectral resolution. Table 1 lists the magnitudes of the pulses used for the three  
3  
4 vibrational bands recorded; the differences of the fields employed reflect the very  
5  
6 different intensities of the three observed bands. The first pulse served the purpose of  
7  
8 eliminating prompt electrons and field ionizing the highest Rydberg states. It was  
9  
10 immediately followed by a second pulse with opposite polarity which produced the  
11  
12 electrons that were detected in the PFI-ZEKE photoelectron spectra. A resolution of  
13  
14 2 - 3 cm<sup>-1</sup> was achieved in the spectra which was sufficient to resolve the rotational  
15  
16 structure of the photoelectron bands of ND<sub>3</sub>. The field-induced shifts of the ionization  
17  
18 potential arising from these pulses were calculated using the procedure described in  
19  
20 Ref. [20] and are listed in Table 1. The VUV wavenumber was determined by  
21  
22 calibrating the wavenumbers of the two dye lasers. This calibration was achieved by  
23  
24 recording the laser-induced fluorescence spectrum of I<sub>2</sub> and optogalvanic spectra of  
25  
26 Ar and Ne. The estimated accuracy of the ionization thresholds determined in this  
27  
28 work is 1 cm<sup>-1</sup>.  
29  
30  
31  
32  
33  
34  
35  
36  
37

## 38 (2.2) Results

39  
40 The experimental PFI-ZEKE photoelectron spectra obtained following single-photon  
41  
42 excitation from the neutral vibronic ground state are shown in panel (a) of Figs. 1, 2  
43  
44 and 3. The Franck-Condon factor is highly unfavourable for the  $v_2^+ = 0$  band relative  
45  
46 to bands of higher  $v_2^+$ , hence a spectrum of lower signal-to-noise ratio is obtained at  
47  
48 that threshold. As is usual in PFI-ZEKE photoelectron spectroscopy, the  
49  
50 wavenumbers of the observed peaks (when corrected for the field ionization shift –  
51  
52 see above) correspond to the differences between the energies of the rovibrational  
53  
54 ionization thresholds in question and the initial levels of the excitation, *i.e.*  
55  
56  
57  
58  
59  
60

$$h\nu = I_0 + G(v_2^+) + F(N^+, K^+) - F(J'', K''), \quad (1)$$

where  $I_0$  is the adiabatic ionization energy,  $G(\nu_2^+)$  is the vibrational energy in the  $\nu_2$  inversion (umbrella bending) mode of the ion (the only mode excited in these spectra) and the  $F$  terms are given by the rigid-rotor expression

$$F(N, K) = BN(N + 1) + (C - B)K^2. \quad (2)$$

for the rotational energies of the ion  $[(N, K) = (N^+, K^+)]$  and neutral ground state  $[(N, K) = (N'', K'')]$ . The values of  $F(N'', K'')$  for the  $\tilde{X}^1A_1'$  ground state of  $\text{ND}_3$  used in the simulations are taken from reference [21].

The general rovibronic selection rules for the photoionization (or for transitions to Rydberg states) of polyatomic molecules derived in Ref. [22] can be expressed as

$$\Gamma_{\text{rve}}^+ \otimes \Gamma_{\text{rve}}'' \otimes \Gamma_e \supseteq \Gamma^*, \quad (3)$$

where  $\Gamma_{\text{rve}}^+$  and  $\Gamma_{\text{rve}}''$  represent the rovibronic symmetries of the cationic and neutral states in the molecular symmetry group  $D_{3h}(\text{M})$ ,  $\Gamma_e$  the symmetry of the photoelectron wave function, (i.e.  $A_1'$  and  $A_1''$  for even- $\ell$  and odd- $\ell$  partial waves, respectively) and  $\Gamma^*$  the dipole moment representation (i.e.  $A_1''$  in  $D_{3h}(\text{M})$ ). For  $\text{ND}_3$  these rovibronic selection rules can be written as

$$\begin{aligned} A_1'' &\leftrightarrow A_1' \\ A_2'' &\leftrightarrow A_2' \\ E'' &\leftrightarrow E' \end{aligned} \quad (4)$$

for even- $\ell$  partial waves and

$$\begin{aligned} A_1'' &\leftrightarrow A_1'' \\ A_1' &\leftrightarrow A_1' \\ A_2'' &\leftrightarrow A_2'' \\ A_2' &\leftrightarrow A_2' \\ E'' &\leftrightarrow E'' \\ E' &\leftrightarrow E' \end{aligned} \quad (5)$$

for odd- $\ell$  partial waves.

A schematic diagram of the rotational energy levels of the  $\tilde{X}^1A_1'$  vibronic ground state of  $\text{ND}_3$  and of the first two out-of-plane bending levels ( $2^0, 2^1$ ; the notation implies  $\nu_2^{\nu_2^+}$ ) of the  $\tilde{X}^2A_2''$  ground state of  $\text{ND}_3^+$  is presented in Fig. 4. Because the

1  
2 out-of-plane bending mode of  $\text{ND}_3$  is of  $a_2''$  symmetry, out-of-plane bending levels  
3  
4 with an even (odd) number of vibrational quanta transform as  $A_1'$  ( $A_2''$ ) and have the  
5  
6 same rovibronic symmetry labels as the  $2^0$  ( $2^1$ ) levels. Distinct rovibronic selection  
7  
8 rules and an overall different rotational structure are thus expected for transitions from  
9  
10 the ground neutral state of  $\text{ND}_3$  to out-of-plane bending levels of  $\text{ND}_3^+$  with even and  
11  
12 odd numbers of vibrational quanta.

13  
14  
15 The general rovibronic photoionization selection rules in Eqs. (3) to (5) are rather  
16  
17 unrestrictive and the full set of transitions predicted using them exceeds the number of  
18  
19 transitions actually observed. To assist with the assignment of the spectra, simulations  
20  
21 were carried out based on the orbital ionization model described in Ref. [23], which  
22  
23 itself is an extension of the Buckingham, Orr and Sichel (BOS) diatomic  
24  
25 photoionization model [24], to predict the strongest lines. The intensity distributions  
26  
27 of the spectra displayed below the experimental spectra in panels (b) of Figs. 1, 2 and  
28  
29 3 were calculated using Equation (6) [23],  
30  
31  
32  
33

$$I(v^+, N^+, K^+, N'', K'') = \rho'' C \sum_{|\lambda''| \leq \ell''} \frac{1}{2\ell'' + 1} Q(\ell'') |C_{\ell'' \lambda''}|^2 \left[ \ell'' |F_{\ell''}^{E, \ell''-1}|^2 + (\ell'' + 1) |F_{\ell''}^{E, \ell''+1}|^2 \right]. \quad (6)$$

34  
35  
36 In Equation (6),  $\rho''$  and  $C$  represent the Boltzmann factor (including nuclear-spin  
37  
38 statistical weight) and a proportionality constant, respectively, and  $\ell''$  represents the  
39  
40 orbital angular momentum quantum number of the different terms of a single-centre  
41  
42 expansion (with expansion coefficients  $C_{\ell'' \lambda''}$ ) of the molecular orbital  $\phi''$  out of which  
43  
44 the photoelectron is ejected.  $F_{\ell''}^{E, \ell}$  is a radial integral and  
45  
46  
47  
48  
49  
50  
51

$$Q(\ell'') = (2N^+ + 1) \begin{pmatrix} N^+ & \ell'' & N'' \\ -K^+ & \lambda'' & K'' \end{pmatrix}, \quad (7)$$

52  
53  
54 where the term in parentheses represents a  $3j$ -symbol (see Ref. [23] for more details).  
55  
56  
57

58  
59 To simulate the relative intensities of the various rotational lines of a given band,  
60  
the product of the squared expansion coefficient  $|C_{\ell'' \lambda''}|^2$  and the term in square

brackets in Eq. (6) were treated as a single parameter, the value of which was adjusted to best reproduce the observed intensities. If it is assumed that the molecular orbital out of which the photoelectron is ejected in the  $\tilde{X}^2A_2'' \leftarrow \tilde{X}^1A_1'$  transition of  $\text{ND}_3$  is a  $p_z$  orbital (i.e.,  $\ell'' = 1, \lambda'' = 0$ ) the sum in Eq. (6) reduces to a single term

$$I(v^+, N^+, K^+, N'', K'') = C'' \chi'' \exp\left(-\frac{E''}{k_B T}\right) (2N'' + 1) g'' \begin{pmatrix} N^+ & 1 & N'' \\ -K^+ & 0 & K'' \end{pmatrix}^2 \quad (8)$$

where  $C''$  is a constant,  $\chi''$  stands for the spin statistical factor and  $g''$  is the degeneracy factor of the ground state rotational levels, i.e.  $2N''+1$  for  $K = 0$  and  $2(2N''+1)$  for  $K \neq 0$  levels. The simulations presented in the panels (b) of Figs. 1, 2 and 3 were made using Eq. (8) assuming a rotational temperature of 15 K.

The pattern of peaks calculated using the orbital ionization model for  $v_2^+ = 0$  (Fig. 1b) is roughly the same as for  $v_2^+ = 2$  (Fig. 3b), because the vibronic symmetry is the same in both cases. The pattern is different for  $v_2^+ = 1$  (Fig. 2b) however, because the  $a_2''$  symmetry ( $D_{3h}$ ) of the  $v_2$  vibrational mode results in a different set of allowed rotational transitions. To assign the experimental spectra, the strong rotational features in the simulated vibrational bands are identified with the strong features in the experimental spectra. Lining up the simulated and experimental spectra allows an initial value for the sum  $I_{v_2^+} = I_0 + G(v_2^+)$  to be estimated. Improved values of  $I_{v_2^+}$  and of the rotational constants  $B^+$  and  $C^+$  of the ion can then be determined by a least-squares fitting method to improve the fit. At the low temperature of the supersonic expansion only low rotational states are populated and centrifugal distortion effects are negligible.

Following a preliminary analysis as described above it was recognised that numerous transitions were observed which could not be identified using the orbital ionization model. The simulations shown in panel (c) of Figs. 1, 2 and 3 assume a relaxation of the orbital restrictions allowing transitions from orbital components of  $f$

1  
2 character in addition to the  $p$  character. As discussed below, such relaxation does not  
3  
4 necessarily reflect the underlying direct ionization cross sections, but was useful in  
5  
6 assigning additional lines.  
7  
8  
9

10  
11  
12 Tables 2, 3 and 4 give the assignments and observed line positions of the rotational  
13  
14 features in each vibrational band. The wavenumbers of the observed bands lie slightly  
15  
16 below the actual ionization thresholds by an amount given by the field-induced shifts  
17  
18 listed in Table 1. The best-fit values of the adiabatic ionization energy, the vibrational  
19  
20 intervals and the rotational constants of  $\text{ND}_3^+$  are given in Table 5 and are compared  
21  
22 to the best values from the literature, or to values extrapolated from the literature (e.g.,  
23  
24 from the work of Kraemer and Špirko [25] in which *ab-initio* calculations are  
25  
26 combined with a fit to experimental data to calculate a potential energy surface for  
27  
28  $\text{NH}_3$  and  $\text{ND}_3$  from which spectroscopic constants can be derived). The experimental  
29  
30 rotational constants and vibrational intervals fall within  $0.1 \text{ cm}^{-1}$  and  $3 \text{ cm}^{-1}$ ,  
31  
32 respectively, of the literature values. The rotational constants for the  $v_2^+ = 0, 1$  levels  
33  
34 can also be compared to values obtained from high resolution REMPI spectra of the  
35  
36  $\tilde{C}'$   $3p$  ( $n = 3$ ) Rydberg state [26], also shown in Table 5. The good agreement  
37  
38 between these values reflects the expected similar geometry between the Rydberg  
39  
40 state and the ion. For the purpose of assigning the photoionization spectrum of  $\text{ND}_3$ ,  
41  
42 the most significant improvement in parameters derived from these measurements is  
43  
44 in the experimental value of the adiabatic ionization potential ( $82261.7(7) \text{ cm}^{-1}$ ),  
45  
46 which is now known with almost two orders of magnitude higher precision than the  
47  
48 previous best value.  
49  
50  
51  
52  
53  
54  
55  
56  
57  
58  
59  
60

The  $\Delta K = 0$  lines in Tables 2 to 4 originating from levels with  $K'' = 0$  are of  
symmetry type  $A'' \leftrightarrow A'$  and are uniquely associated with even- $\ell$  photoelectron partial

1 waves (see Eq. 4). The other lines are of type  $E \leftrightarrow E$  and could in principle be  
 2  
 3 described as associated with either even- $\ell$  or odd- $\ell$  partial waves because transitions  
 4  
 5 involving near-degenerate  $E''$  and  $E'$  levels are not resolved. [Note that although we  
 6  
 7 refer to ‘photoelectron partial waves’ here, the actual excitation in a PFI-ZEKE  
 8  
 9 photoelectron experiment is to a high Rydberg state with a given  $\ell$  value rather than a  
 10  
 11 true continuum]. As discussed previously [2,17], even- $\ell$  partial waves are likely to  
 12  
 13 dominate the spectra and, in fact, all of the observed transitions can be explained by  
 14  
 15 using even- $\ell$  partial waves alone. Four  $K'' = 0$  transitions are unambiguously  
 16  
 17 identified that can *only* be explained assuming even- $\ell$  photoelectron partial waves,  
 18  
 19 and these include strong transitions in all three vibrational bands, most notably the  $1_0$   
 20  
 21  $A_1'' \leftarrow 0_0 A_1'$  transition at  $82270.4 \text{ cm}^{-1}$  in the  $\nu_2^+ = 0$  band, the  $0_0 A_1' \leftarrow 1_0 A_1''$   
 22  
 23 transition at  $82936.4 \text{ cm}^{-1}$  in the  $\nu_2^+ = 1$  band and the  $1_0 A_1'' \leftarrow 0_0 A_1'$  transition at  
 24  
 25  $83665.7 \text{ cm}^{-1}$  in the  $\nu_2^+ = 2$  band. This predominance of even- $\ell$  partial waves in the  
 26  
 27 single-photon ionization of  $\text{ND}_3$  substantiates our previous findings derived from the  
 28  
 29 spectra of  $\text{NH}_3$  [2],  $\text{ND}_2\text{H}$  and  $\text{NH}_2\text{D}$  [17]. In general the strongest features are  
 30  
 31 identified as  $\Delta K = K^+ - K'' = 0$ .  
 32  
 33  
 34  
 35  
 36  
 37  
 38  
 39  
 40  
 41  
 42

43 The two ( $\nu_2^+ = 1$ ) or three ( $\nu_2^+ = 0, 2$ ) strongest features predicted by the  
 44  
 45 orbital ionization model for each vibrational band are also observed as strong features  
 46  
 47 in the experimental spectra (Figs. 1, 2 and 3) but with some differences in the relative  
 48  
 49 intensities. As discussed above, several additional transitions are observed for which  
 50  
 51 no intensity is predicted by the orbital ionization model, particularly in the  $\nu_2^+ = 1$  and  
 52  
 53 2 bands. The spectra calculated using the relaxed selection rules shown in panel (c) of  
 54  
 55 Figs. 1 to 3 contain nearly all of the observed features, but not always with the correct  
 56  
 57 relative intensities. The inclusion of higher- $\ell''$  components in the simulations (Eq. (6))  
 58  
 59 is therefore unlikely to represent the direct ionization cross-sections.  
 60

1  
2 One factor contributing to some of the intensity discrepancies may be the  
3  
4 uncertainty about the relative populations of the neutral molecule rotational levels in  
5  
6 the supersonic jet. For  $\text{NH}_2\text{D}$  and  $\text{ND}_2\text{H}$  it was previously found [17] that there was  
7  
8 significant nuclear-spin-state inter-conversion in the supersonic expansion,  
9  
10 attributable to an initial clustering near the jet orifice. The simulations shown in Figs.  
11  
12 1 - 3 assume a rotational temperature of 15 K; changing the temperature or the degree  
13  
14 of nuclear-spin-state inter-conversion does not improve the fit especially for the weak  
15  
16 features observed on the high wavenumber side of the  $\nu_2^+ = 1$  and 2 bands.  
17  
18  
19  
20

21 The most likely explanation for the differences to the predictions of the orbital  
22  
23 ionization model lies in the channel interactions between different Rydberg series. As  
24  
25 has been well documented elsewhere [6, 7, 27, 28] the pseudo continuum of high- $n$   
26  
27 Rydberg states detected in PFI-ZEKE photoelectron experiments below a particular  
28  
29 ionization threshold may interact with either bound Rydberg series converging to  
30  
31 higher energy thresholds, or the continua associated with lower energy thresholds, and  
32  
33 thereby borrow intensity from the stronger transitions to those interacting channels.  
34  
35 Such channel interactions are not incorporated into the BOS orbital ionization model,  
36  
37 but have been explained in our previous study of the  $(2 + 1')$  MATI spectra of  $\text{NH}_3$  via  
38  
39 the  $\tilde{B}$  and  $\tilde{C}$  states using multichannel quantum defect theory [6, 7]. Figures 1(d) to  
40  
41 3(d) show the photoionization spectra recorded in the same regions as the PFI-ZEKE  
42  
43 photoelectron spectra by detecting ions produced by autoionization as a function of  
44  
45 the laser wavenumber. These spectra indicate that the unexpectedly intense lines in  
46  
47 the PFI-ZEKE photoelectron spectra always coincide with autoionization resonances  
48  
49 in the photoionization spectrum. For example the strong  $3_1 \leftarrow 2_1$  and  $3_3 \leftarrow 0_0$  lines in  
50  
51 the 0 - 0 band correspond to strong features in the photoionization spectrum near  
52  
53  $82295 \text{ cm}^{-1}$ ; these photoionization resonances are tentatively assigned (see below) as  
54  
55 transitions to  $\nu_2^+ = 3$ ,  $n = 8$  Rydberg states. The strong  $4_2 \leftarrow 2_2$  feature in the  $\nu_2^+ = 1$   
56  
57  
58  
59  
60

1  
2 band appears to coincide with a strong photoionization resonance near  $83020\text{ cm}^{-1}$   
3  
4 which is also believed to involve transitions to a group of  $v_2^+ = 3$  autoionizing states,  
5  
6 and the features at the high wavenumber end of the  $v_2^+ = 2$  band of the photoelectron  
7  
8 spectra may also be “borrowing” intensity from the overlapping autoionizing features.  
9  
10 Such intensity borrowing, however, can only occur if the autoionizing features share a  
11  
12 common ground state with the perturbed line of the PFI-ZEKE spectrum.  
13  
14  
15  
16  
17  
18

### 19 (3) MQDT simulation of the photoionization spectrum of $\text{ND}_3$

20  
21  
22  
23 The spectroscopic constants derived from the rotationally resolved PFI-ZEKE  
24  
25 photoelectron spectra of  $\text{ND}_3$  were used to carry out a simulation of the  
26  
27 photoionization spectrum using Multichannel Quantum Defect Theory (MQDT). The  
28  
29 methodology employed is described in more detail elsewhere [16] and follows closely  
30  
31 the theory described in references [6, 7, 29, 30]. In this scattering-theory approach the  
32  
33 long-range ‘channels’ define the set of possible quantum states of the system when the  
34  
35 electron is at long range from the ion core. The electron may either be a free electron  
36  
37 with given angular momentum  $\ell$  dissociating from a quantum-state specified ion  
38  
39 core  $N^+$ ,  $K^+$ ,  $v^+$  (an ‘open’ channel), or a Rydberg electron of specified  $\ell$  bound to an  
40  
41 ion core  $N^+$ ,  $K^+$ ,  $v^+$  (a ‘closed’ channel). In both cases the total angular momentum  
42  
43 quantum number excluding spin,  $N$ , is also specified. For closed and open channels  
44  
45 the total energy lies respectively below or above the threshold for the particular  $N^+$ ,  
46  
47  $K^+$ ,  $v^+$  ion core state. [To simplify notation below,  $v_2^+$  is replaced by  $v^+$ , as channels  
48  
49 with non-zero values of the other vibrational quantum numbers are omitted, and thus  
50  
51 the  $v_2$  mode is assumed to be the only active one.]  
52  
53  
54  
55  
56  
57  
58  
59  
60

The total photoionization cross section at a given energy is equal to the sum of partial photoionization cross sections into the set of  $N_O$  open channels, summed over all populated initial levels. The photoionization spectrum is calculated by evaluating the total cross section as a function of energy on a fine energy grid ( $0.01 \text{ cm}^{-1}$  in the present case). The partial photoionization cross section at energy  $E$  for excitation from an initial rotational level  $J''$ ,  $K''$  into the open channel  $N^+ K^+ v^+ \ell N$  (represented by the label  $i$ ) is given by

$$\sigma_{J''K'' \rightarrow i}(E) = \frac{4\pi^2 \zeta \omega}{3(2J'' + 1)} \sum_N |D_i^{(N)}(E)|^2, \quad (9)$$

where  $D_i^{(N)}(E)$  is the reduced transition dipole moment between the initial state and the final channel  $|i\rangle$ ,  $\zeta$  is the fine structure constant, and  $\omega$  is the photon energy (atomic units). The energy-dependent reduced transition dipole moments are related to the transition dipole moments in the rovibronic eigenchannel representation,  $D_\alpha^{(N)}$ , using the expression,

$$D_i^{(N)} = \sum_\rho e^{i\eta_\rho} T_{i\rho} e^{i\pi\rho} \sum_\alpha D_\alpha^{(N)} A_{\alpha\rho}. \quad (10)$$

In this equation,  $\rho$  labels one of the  $N_O$  independent solutions of the Schrödinger equation at this energy  $E$ , and  $\alpha$  labels the eigenchannels defined in the expansion

$$\Psi_\rho = \sum_\alpha A_{\alpha\rho}(E) \Psi_\alpha(E). \quad (11)$$

The eigenchannel wavefunction  $\Psi_\alpha$  is given by

$$\Psi_\alpha = \sum_i U_{i\alpha} [f_i - g_i \tan(\pi\mu_\alpha)] |i\rangle, \quad (12)$$

where  $f_i$  and  $g_i$  are regular and irregular radial Coulomb functions, and  $|i\rangle$  is the ion core and electronic angular momentum parts of the wavefunctions which characterize each channel  $i$ .  $\mu_\alpha$  is the eigenchannel quantum defect and  $U_{i\alpha}$  is the transformation matrix between the long-range basis and the eigenchannel basis.

A further frame transformation relates the transition moments in equation (10) to a set of transition moments  $\langle NK\ell\lambda|d|J''K''\lambda''\rangle$  defined in a close-coupled channel (or short-range) basis equivalent to a Hund's case (b) representation

$$D_{\alpha}^{(N)} = \sum_i (U_{\alpha i}^T)^{(N)} \sum_{\ell\lambda} \langle N^+K^+ | K\lambda \rangle^{(\ell N)} \left[ \int dQ \langle v^+ | Q \rangle^{(N^+K^+)} \langle NK\ell\lambda|d|J''K''\lambda''\rangle \langle Q|v''\rangle^{(N''K'')} \right] \quad (13)$$

$\langle v^+ | Q \rangle^{N^+K^+}$  and  $\langle Q|v''\rangle^{N''K''}$  are vibrational wavefunctions and the factors in square brackets in Eq. (13), including the vibrational overlap integral, are treated as variable input parameters in the present calculations.

To determine the transformation matrix  $U_{i\alpha}$  in Eqs. (12) and (13) the rovibronic quantum defect matrix in the long-range basis  $\mu_{ii'}$  is constructed by relating it to a set of input quantum defects defined in the close-coupled Hund's case (b) basis,

$$\mu_{ii'} \equiv \mu_{v^+N^+K^+\ell; v''N''K''\ell'}^{(N)} = \sum_{K\lambda} \sum_{K'\lambda'} \langle N^+K^+ | K\lambda \rangle^{(\ell N)} \left[ \int dQ \langle v^+ | Q \rangle \mu_{\ell\lambda, \ell'\lambda'}(Q) \langle Q|v''\rangle \right] \langle \lambda'K' | N''K'' \rangle^{(\ell' N)}, \quad (14)$$

where the  $\mu_{\ell\lambda, \ell'\lambda'}$  matrix elements are treated as input parameters, determined in this work principally by *ab-initio* calculation [16]. The quantum defect matrix  $\mu_{ii'}$  is then diagonalized, as in ref [29], to determine the  $U_{i\alpha}$  elements as the eigenvectors and the eigenchannel quantum defects  $\mu_{\alpha}$  as the eigenvalues.

The  $T$  matrix in Eq. (10) is given by

$$T_{i\rho}(E) = \sum_{\alpha} U_{i\alpha}^{(N)} \cos[\pi(-\tau_{\rho} + \mu_{\alpha}^{(N)})] A_{\alpha\rho} \quad (15)$$

and the coefficients  $A_{\alpha\rho}$  and scattering phases  $\tau_{\rho}$  are determined from the generalized eigenvalue equation [29]:

$$\begin{aligned} \Gamma \mathbf{A} &= \tan(\pi\tau) \Lambda \mathbf{A} \\ \Gamma_{i\alpha} &= U_{i\alpha}^{(N)} \sin[\pi(v_i + \mu_{\alpha}^{(N)})] \quad \text{for } i \text{ closed} \\ \Gamma_{i\alpha} &= U_{i\alpha}^{(N)} \sin(\pi\mu_{\alpha}^{(N)}) \quad \text{for } i \text{ open} \\ \Lambda_{i\alpha} &= 0 \quad \text{for } i \text{ closed} \\ \Lambda_{i\alpha} &= U_{i\alpha}^{(N)} \cos(\pi\mu_{\alpha}^{(N)}) \quad \text{for } i \text{ open} \end{aligned} \quad (16)$$

$v_i$  is the effective principal quantum number in channel  $i$  at the total energy  $E$ .

The expression in the square brackets in Eq. (14) determines the coupling between channels associated with different vibrational thresholds of the  $\text{ND}_3^+$  ion, and is thus responsible for vibrational autoionization. The coupling between channels with different  $v^+$  quantum numbers is assumed, for the purposes of these calculations, to be negligible for  $\Delta v^+ > 1$ . For the  $\Delta v^+ = 1$  matrix elements, rather than integrating over the vibrational wavefunction, we use the following harmonic approximation to the matrix elements [31] (which effectively ignores the very small dependence of the vibrational wavefunctions on the rotational quantum numbers  $N^+$  and  $K^+$ );

$$\mu_{\ell\lambda v\ell'\lambda'v'} = \int dQ \langle v^+ | Q \rangle^{(N^+K^+)} \mu_{\ell\lambda\ell'\lambda'}(Q) \langle Q | v^{+'} \rangle^{(N^{+'}K^{+'})} = \left( \frac{d\mu_{\ell\lambda\ell'\lambda'}}{dQ} \right)_e \left[ \frac{h}{8\pi^2 c \omega} \right]^{\frac{1}{2}} (v^+)^{\frac{1}{2}} \quad (17)$$

1  
2 where  $v^+$  is the vibrational quantum number of the closed channel undergoing  
3 autoionization, and  $\omega$  is the vibrational frequency. There is also a symmetry selection  
4 rule applying to these off-diagonal matrix elements which restricts the number of  $\ell\lambda -$   
5  $\ell'\lambda'$  pairs for which the derivative in Eq. (17) needs to be evaluated [16]. Note that  
6  
7 this rule is applied in  $D_{3h}$  symmetry in which, for example,  $p\pi$  and  $d\delta$  correlate to the  
8  
9 same representation. Hence the non-zero elements include both pairs with opposite  
10  
11 parity (e.g.,  $p\pi - d\pi$ ) as well as one pair with the same parity ( $d\pi - d\delta$ ).  
12  
13  
14  
15  
16  
17  
18  
19  
20  
21

22 Equation (17) ignores all vibrational modes other than the out-of-plane bend and is a  
23 purely harmonic approximation. Evaluation of (17) requires knowledge of how the  
24 short-range electronic quantum-defect matrix elements  $\mu_{\ell\lambda\ell'\lambda'}$  vary with the  $v_2^+$  normal  
25 vibrational coordinate at the equilibrium geometry. The variation is determined in this  
26 work by *ab-initio* calculation as described elsewhere [16]. For the matrix elements  
27  
28 *diagonal* in the  $v^+$  quantum number, we set the integral over the vibrational co-  
29  
30 ordinate equal to the value at the planar equilibrium geometry, assuming only a small  
31  
32 variation of the quantum defects over the range of geometries over which the  
33  
34 vibrational wavefunctions of the low vibrational levels extend.  
35  
36  
37  
38  
39  
40  
41  
42  
43  
44  
45

46 The diagonal quantum defects employed in the MQDT calculation  $\mu_{\ell\lambda\ell\lambda}$  have been  
47 slightly adjusted from the *ab-initio* values to give a better fit to the photoionization  
48 spectrum of  $\text{NH}_3$  [16] and are listed together with the off-diagonal elements and the  
49 off-diagonal vibrational integrals (from Eq (17)) in Table 6. The best match to the  
50  
51 experimental intensities is obtained by setting all the transition dipole moment  
52  
53 parameters in Eq. (13) to zero, except for those involving  $\ell = 0$ . Note however that  
54  
55  
56  
57  
58  
59  
60 because there is substantial  $\ell = 0 - \ell = 2$  mixing in this system the Rydberg states

1  
2 populated have a mixture of  $ns$  and  $nd$  character. The rotational temperature in the  
3  
4 supersonic expansion for the experiments of Ref [2] was estimated to be 5 - 10 K, and  
5  
6 therefore the spectrum is calculated as a sum of partial photoionization cross sections  
7  
8 out of the 6 lowest energy levels of  $\text{ND}_3$  which are the only ones significantly  
9  
10 populated. The channels included in the calculation were those with  $v^+ = 0$  to 3 and  $\ell$   
11  
12  $= 0$  to 2. The partial photoionization cross section calculation (Eq. (9)) is carried out  
13  
14 for a specific total angular momentum  $N$ , and this, together with symmetry  
15  
16 considerations [7], restricts the number of rotational quantum numbers  $N^+ K^+$  that  
17  
18 need to be included.  
19  
20  
21  
22  
23  
24  
25

26 Fig. 5 compares the MQDT simulation obtained with an overview of the  
27  
28 experimental photoionization spectrum from reference [2]. The simulation has been  
29  
30 colour coded according to the initial rotational level from which the transitions  
31  
32 originate. The strong features observed at either end of the experimental spectrum are  
33  
34 well reproduced in the simulated spectrum and much of the structure observed in the  
35  
36 central region of the spectrum is also reproduced. Figs. 6 and 7 give expanded views  
37  
38 of two regions of the spectrum. The degree of qualitative match between simulation  
39  
40 and experiment is extremely sensitive to the diagonal elements of the quantum defect  
41  
42 matrix used as input and to the positions of the ro-vibrational ionic thresholds. Most  
43  
44 of the features in the calculated spectrum are identified as autoionizing levels  
45  
46 belonging to series converging on the  $v_2^+ = 1$  state of the ion, but a number of  
47  
48 transitions belonging to higher vibrational levels ( $v_2^+ = 2$  and 3) have also been  
49  
50 identified as shown in Fig. 5, including the  $n = 10$ ,  $v_2^+ = 2$ ,  $3_0 A_1'' \leftarrow 0_0 A_1'$  transition,  
51  
52 three transitions ( $n = 9, 11, 13$ ) of the  $v_2^+ = 2$ ,  $1_0 A_1'' \leftarrow 0_0 A_1'$  series and the intense  $n$   
53  
54  $= 9$ ,  $v_2^+ = 3$ ,  $1_1 E'' \leftarrow 1_1 E'$  transition at the high-wavenumber end of the spectrum.  
55  
56  
57  
58  
59  
60

These vibrational assignments were made by allowing the transition moments to one

1  
2 particular vibrational channel (selected in turn) to be non-zero, while setting all  
3  
4 transition moments to other vibrational channels to zero.  
5  
6

7 Overall the assignment and detailed identification of Rydberg series in the  $\nu_2^+$   
8  
9 = 1 region of the  $\text{ND}_3$  high-resolution photoionization spectrum is less straightforward  
10  
11 than for the  $\text{NH}_3$  spectrum [2]. The region near the  $\nu_2^+ = 0$  threshold, where series  
12  
13 were readily identified in the photoionization spectrum of  $\text{NH}_3$ , is quite weak for  $\text{ND}_3$ ,  
14  
15 and at higher wavenumber there are no obvious series appearing in between the  $\nu_2^+ =$   
16  
17 0 and  $\nu_2^+ = 1$  thresholds (whereas for  $\text{NH}_3$  the  $1_0 A_2' \leftarrow 0_0 A_2''$  series dominates this  
18  
19 region of the spectrum). Nevertheless, it is possible to make use of the likely  
20  
21 correlation between the transitions that are strong in the PFI-ZEKE photoelectron  
22  
23 spectra of  $\text{ND}_3$  and those series that have high intensity in the photoionization spectra.  
24  
25 As illustration, Figure 8 displays one long progression that can be assigned as a series  
26  
27 converging to the  $\nu_2^+ = 1$ ,  $1_1 E' \leftarrow 2_1 E''$  rovibronic threshold which corresponds to a  
28  
29 strong transition in the  $\nu_2^+ = 1$  PFI-ZEKE photoelectron spectrum at  $82967 \text{ cm}^{-1}$ . The  
30  
31  $1_1 E'' \leftarrow 1_1 E'$  transition also appears with high intensity in the  $\nu_2^+ = 1$  band of the PFI-  
32  
33 ZEKE photoelectron spectrum at  $82946 \text{ cm}^{-1}$  and a series converging to this threshold  
34  
35 can be identified in the photoionization spectrum of  $\text{ND}_3$  from  $n = 17 - 23$ , and is well  
36  
37 reproduced in the MQDT simulation shown in Fig. 7.  
38  
39  
40  
41  
42  
43  
44  
45

46 The series and fractions of series identified, assigned and simulated in the  
47  
48 high-resolution photoionization spectrum of  $\text{ND}_3$  are summarised in Table 7. The  
49  
50 central region of the spectrum between  $82450 \text{ cm}^{-1}$  and  $82850 \text{ cm}^{-1}$  is chosen for  
51  
52 illustration and shown with series assignments in Fig. 8. A large percentage of the  
53  
54 strong spectral features can be assigned by the MQDT simulation, which is a powerful  
55  
56 tool in the interpretation of such complex photoionization spectra.  
57  
58  
59  
60

#### 4. Conclusions

1  
2  
3  
4 The work described in this paper, when coupled with our previous work in references  
5 [2, 6, 7, 16, 17], provides information on the several ro-vibrational ionization  
6  
7 thresholds of four isotopomers of ammonia. The band origins for the observed  
8  
9 transitions are collected in Table 8. Rotational constants and vibrational intervals for  
10  
11 the  $\text{ND}_3^+$  ion have also been derived from experiment for the first time. The  
12  
13 underlying motivation for this work was to extend the assignment of the high-  
14  
15 resolution photoionization spectrum, and MQDT calculations carried out on  $\text{NH}_3$  to  
16  
17 the photoionization spectrum of  $\text{ND}_3$ . The good agreement using the same set of  
18  
19 electronic parameters for both isotopomers, despite the very different rotational and  
20  
21 vibrational constants, nuclear spin statistical weights and vibronic dynamics indicates  
22  
23 the reliability of these parameters. Whereas the agreement between the measured and  
24  
25 calculated line positions is good, the intensities are not described so well by the  
26  
27 calculations. We attribute the discrepancies to the fact that predissociation has not  
28  
29 been included in the calculations, even though it is known that many Rydberg states  
30  
31 of ammonia are predissociative.  
32  
33  
34  
35  
36  
37  
38  
39  
40  
41

42 The ammonia molecule is a model system with which to study photoionization in  
43  
44 polyatomic molecules and reveals many fascinating features; the studies presented in  
45  
46 this work and references [2,16,17] have substantially extended the understanding of  
47  
48 the highly excited states of ammonia, while still leaving room for detailed  
49  
50 considerations of the predissociation of these states in the future, and of the  
51  
52 competition with autoionization.  
53  
54  
55  
56  
57  
58  
59  
60

## Acknowledgements

We are grateful for financial support of this work to the Swiss National Science Foundation (project No 200020-125030), to the Petroleum Research Fund of the American Chemical Society, and to the Engineering and Physical Sciences Research Council.

## References

- [1] J. W. Rabalais, L. Karlsson, L. O. Werme, T. Bergmark and K. Siegbahn, J. Chem. Phys. **58**, 3370 (1973).
- [2] R. Seiler, U. Hollenstein, T. P. Softley and F. Merkt, J. Chem. Phys. **118**, 10024 (2003).
- [3] B. Niu and M. G. White, J. Chem. Phys. **104**, 2136 (1996).
- [4] M. Bahng, X. Xing, S. J. Baek, and C. Y. Ng, J. Chem. Phys. **123**, 084311 (2005).
- [5] W. Habenicht, G. Reiser and K. Müller-Dethlefs, J. Chem. Phys. **95**, 4809 (1991).
- [6] H. Dickinson, D. Rolland and T. P. Softley, Phil. Trans. Roy. Soc. Lond. A **355**, 1585 (1997).
- [7] H. Dickinson, D. Rolland and T. P. Softley, J. Phys. Chem. A **105**, 5590 (2001).
- [8] S. R. Langford, A. J. Orr-Ewing, R. A. Morgan, C. M. Western, M. N. R. Ashfold, A. Rijkenberg, C. R. Scheper, W. J. Buma and C. A. de Lange, J. Chem. Phys. **108**, 6667 (1998).
- [9] D. T. Cramb and S. C. Wallace, J. Chem. Phys., **101**, 6523 (1994).
- [10] J. H. Glowina, S. J. Riley, S. D. Colson and G. C. Nieman, J. Chem. Phys. **73** 4296 (1980).

- 1  
2 [11] W. E. Conaway, R. J. S. Morrison, and R. N. Zare, Chem. Phys. Lett. **113** 429  
3  
4 (1985).  
5  
6 [12] C. A. Raptis and S. T. Pratt, J. Chem. Phys. **115**, 2483 (2001).  
7  
8 [13] C. A. Raptis, J. A. Bacon and S. T. Pratt, J. Chem. Phys. **112**, 2815 (2000).  
9  
10 [14] M. N. R. Ashfold, R. N. Dixon, N. Little, R. J. Stickland and C. M. Western, J.  
11  
12 Chem. Phys. **89**, 1754 (1988).  
13  
14 [15] P. Hockett, M. Staniforth, K. L. Reid and D. Townsend, Phys. Rev. Lett. **102**,  
15  
16 253002 (2009).  
17  
18 [16] L. Duggan, T. P. Softley, M. S. Child, M. Hiyama, J. Tennyson, U. Hollenstein,  
19  
20 F. Merkt, To be submitted (2009).  
21  
22 [17] U. Hollenstein, F. Merkt, L. Meyer, R. Seiler, T. P. Softley and S. Willitsch, Mol.  
23  
24 Phys. **105**, 1711 (2007).  
25  
26 [18] S. S. Lee and T. Oka, J. Chem. Phys. **94**, 1698 (1991).  
27  
28 [19] F. Merkt, A. Osterwalder, R. Seiler, R. Signorell, H. Palm, H. Schmutz and R.  
29  
30 Gunzinger, J. Phys. B **31**, 1705 (1998).  
31  
32 [20] U. Hollenstein, R. Seiler, H. Schmutz, M. Andrist and F. Merkt, J. Chem. Phys.  
33  
34 **115**, 5461 (2001).  
35  
36 [21] M. Carlotti, G. DiLonardo, S. N. Murzin and O. Stepanov, J. Mol. Spec. **147**, 71  
37  
38 (1991).  
39  
40 [22] R. Signorell and F. Merkt, Mol. Phys. **92**, 793 (1997).  
41  
42 [23] S. Willitsch and F. Merkt, Int. J. Mas. Spectrom. **245**, 14 (2005).  
43  
44 [24] A. D. Buckingham, B. J. Orr and J. M. Sichel, Phil. Trans. Roy. Soc. London A  
45  
46 **268**, 147 (1970).  
47  
48 [25] W. P. Kraemer and V. Špirko, J. Mol. Spec. **153**, 276 (1992).  
49  
50 [26] M. Nolde, K.-H. Weitzel and C. M. Western, Phys. Chem. Chem. Phys. **7**, 1527  
51  
52 (2005).  
53  
54  
55  
56  
57  
58  
59  
60

[27] F. Merkt and T. P. Softley, *Int. Rev. Phys. Chem.* **12**, 205 (1993) .

[28] T. P. Softley, *Int. Rev. Phys. Chem.* **23**, 1 (2004).

[29] N. Y. Du and C. H. Greene, *J. Chem. Phys.* **85**, 5430 (1986).

[30] S. J. Brownbill and T. P. Softley, *Mol. Phys.* **103**, 2347 (2005).

[31] Ch. Jungen and S. T. Pratt, *J. Chem. Phys.* **106**, 9529 (1997).

[32] W. E. Thompson and M. E. Jacox, *J. Chem. Phys.* **114**, 4846 (2001).

### Table and Figure Captions

**Figure 1** (a) PFI-ZEKE photoelectron spectrum of the  $\tilde{X}^+ \ ^2A_2'' (v_2^+ = 0) \leftarrow \tilde{X} \ ^1A_1'$  transition of ND<sub>3</sub>. The lines are assigned using the notation  $N^+_{K^+} \leftarrow N''_{K''}$  (b) Simulation of the PFI-ZEKE photoelectron spectrum using the orbital ionization model (Eq. 8). (c) Simulation based on a less restrictive photoionization model. (d) Experimental photoionization spectrum of ND<sub>3</sub>.

**Figure 2** (a) PFI-ZEKE photoelectron spectrum of the  $\tilde{X}^+ \ ^2A_2'' (v_2^+ = 1) \leftarrow \tilde{X} \ ^1A_1'$  transition of ND<sub>3</sub>. The lines are assigned using the notation  $N^+_{K^+} \leftarrow N''_{K''}$  (b) Simulation of the PFI-ZEKE photoelectron spectrum using the orbital ionization model (Eq. 8). (c) Simulation based on a less restrictive photoionization model. (d) Experimental photoionization spectrum of ND<sub>3</sub>.

**Figure 3:** (a) PFI-ZEKE photoelectron spectrum of the  $\tilde{X}^+ \ ^2A_2'' (v_2^+ = 2) \leftarrow \tilde{X} \ ^1A_1'$  transition of ND<sub>3</sub>. The lines are assigned using the notation  $N^+_{K^+} \leftarrow N''_{K''}$  (b) Simulation of the PFI-ZEKE photoelectron spectrum using the orbital ionization

1  
2 model (Eq. 8). (c) Simulation based on a less restrictive photoionization model. (d)  
3  
4 Experimental photoionization spectrum of ND<sub>3</sub>.  
5  
6  
7  
8  
9

10 **Figure 4:** Energy level diagram showing schematically the rotational levels of the  
11 lowest vibrational level of the  $\tilde{X} ({}^1A_1')$  ground state of ND<sub>3</sub> (bottom panel) and of out-  
12 of-plane bending levels of the  $\tilde{X}^+ ({}^2A_2'')$  ground state of ND<sub>3</sub><sup>+</sup>, with even values of  $\nu_2^+$   
13 (top left panel) and odd values of  $\nu_2^+$  (top right panel). The rovibronic symmetry  
14 labels of all levels in the  $D_{3h}(M)$  molecular symmetry group is indicated next to the  
15 levels.  
16  
17  
18  
19  
20  
21  
22  
23  
24  
25  
26

27 **Figure 5:** Comparison of the photoionization spectrum of ND<sub>3</sub> (bottom trace, from  
28 Ref. [2]) and the MQDT simulation (top trace) calculated using quantum defects from  
29 reference [16]: the separate contributions from each initial rotational state are colour  
30 coded.  
31  
32  
33  
34  
35  
36  
37  
38

39 **Figure 6:** Expanded view of the MQDT simulation (top trace) of the ND<sub>3</sub>  
40 photoionization spectrum (bottom trace, ref [2]). The simulated spectrum was  
41 computed using quantum defects from reference [16]: the  $\nu_2^+ = 1$  region is dominated  
42 by a series of transitions originating from the  $1_1 E'$  ground state level converging to  
43 the  $\nu^+ = 1, 1_1 E' \leftarrow 2_1 E''$  rovibronic threshold.  
44  
45  
46  
47  
48  
49  
50  
51  
52  
53  
54

55 **Figure 7:** Expanded view of the MQDT simulation (top trace) of the ND<sub>3</sub>  
56 photoionization spectrum (bottom trace, ref [2]). The simulated spectrum was  
57 computed using quantum defects from reference [16]:  $\nu_2^+ = 1$  region showing a part of  
58 the Rydberg series converging to the  $1_1 E' \leftarrow 1_1 E''$  rovibronic threshold.  
59  
60

1  
2  
3  
4 **Figure 8:** Example of series assignments based on the MQDT calculations in a  
5 selected region of the high resolution photoionization spectrum of ND<sub>3</sub> (reported in  
6 Ref [2].)  
7  
8  
9

10  
11  
12  
13  
14 **Table 1:** Two-pulse sequences used to record the PFI-ZEKE photoelectron spectra of  
15 ND<sub>3</sub>. The shifts of the ionization thresholds were estimated as described in reference  
16 [20].  
17  
18  
19

20  
21  
22 **Table 2:** Assignment of rotational lines (in the notation  $N^+_{\kappa^+} \leftarrow N''_{\kappa''}$ ) of the  $v_2^+ = 0$   
23 band of the PFI-ZEKE photoelectron spectrum of ND<sub>3</sub>. The reported line positions in  
24 the first column have not been corrected for the shift due to the pulsed field  
25 ionization. The field-free thresholds can be obtained by adding  $1.7 \text{ cm}^{-1}$  to each of the  
26 numbers in column 1 (using the data presented in Table 1.) The calculated  
27 wavenumbers  $\tilde{\nu}_{\text{calc}}$  are obtained from Eqs. (1) and (2) using the best fit rotational  
28 constants, vibrational intervals and the ionization energy given in Table 5.  
29  
30  
31  
32  
33  
34  
35  
36  
37  
38  
39  
40  
41

42 **Table 3:** Assignment of rotational lines (in the notation  $N^+_{\kappa^+} \leftarrow N''_{\kappa''}$ ) of the  $v_2^+ = 1$   
43 band of the PFI-ZEKE photoelectron spectrum of ND<sub>3</sub>. The reported line positions in  
44 the first column have not been corrected for the shift due to the pulsed field  
45 ionization. The field-free thresholds can be obtained by adding  $1.5 \text{ cm}^{-1}$  to each of the  
46 numbers in column 1 (using the data presented in Table 1.) The calculated  
47 wavenumbers  $\tilde{\nu}_{\text{calc}}$  are obtained from Eqs. (1) and (2) using the best fit rotational  
48 constants, vibrational intervals and the ionization energy given in Table 5.  
49  
50  
51  
52  
53  
54  
55  
56  
57  
58  
59  
60

1  
2  
3  
4  
5 **Table 4:** Assignment of rotational lines (in the notation  $N^+_{K^+} \leftarrow N''_{K''}$ ) of the  $v_2^+ = 2$   
6  
7 band of the PFI-ZEKE photoelectron spectrum of  $\text{ND}_3$ . The reported line positions in  
8  
9 the first column have not been corrected for the shift due to the pulsed field  
10  
11 ionization. The field-free thresholds can be obtained by adding  $1.45 \text{ cm}^{-1}$  to each of  
12  
13 the numbers in column 1 (using the data presented in Table 1.) The calculated  
14  
15 wavenumbers  $\tilde{\nu}_{\text{calc}}$  are obtained from Eqs. (1) and (2) using the best fit rotational  
16  
17 constants, vibrational intervals and the ionization energy given in Table 5.  
18  
19  
20  
21  
22  
23  
24  
25  
26  
27

28 **Table 5:** Spectroscopic parameters of  $\text{ND}_3/\text{ND}_3^+$ . Parameters labelled 'Expt' are  
29  
30 from the present work, while those labelled 'REMPI' are from the 2 + 1 REMPI  
31  
32 studies of the  $\tilde{C}'$  state of  $\text{ND}_3$  [26]. Other values are determined as follows:  
33  
34

35 (a) Theoretically determined from an adjusted *ab-initio* potential surface [25].<sup>(b)</sup>  
36  
37 Infrared spectrum of  $\text{ND}_3^+$  recorded in solid neon [31].<sup>(c)</sup> Calculated using the  
38  
39 equation  $C_{0(\text{ND}_3)} \approx \frac{1}{2} C_{0(\text{NH}_3)}$ .<sup>(d)</sup> Calculated using the  $C_2 - C_1$  and  $C_1 - C_0$  values in  
40  
41 reference [25]. (e) Experimental measurement from REMPI studies in ref [8].  
42  
43  
44  
45  
46  
47

48 **Table 6:** Diagonal and off-diagonal elements of the quantum defect matrix used in  
49  
50 the MQDT simulations (from ref [16]). The final row lists the vibrationally integrated  
51  
52 off-diagonal elements as given in Eq (17).  
53  
54  
55  
56  
57

58 **Table 7** Summary of series or parts of series identified in the high-resolution  
59  
60 photoionization spectrum of  $\text{ND}_3$ .

**Table 8** Ionization energies (band origins for transitions to specific vibrational thresholds) derived from the present work and references [2,16,17] for  $\text{NH}_3$ ,  $\text{NH}_2\text{D}$ ,  $\text{NHD}_2$  and  $\text{ND}_3$ .

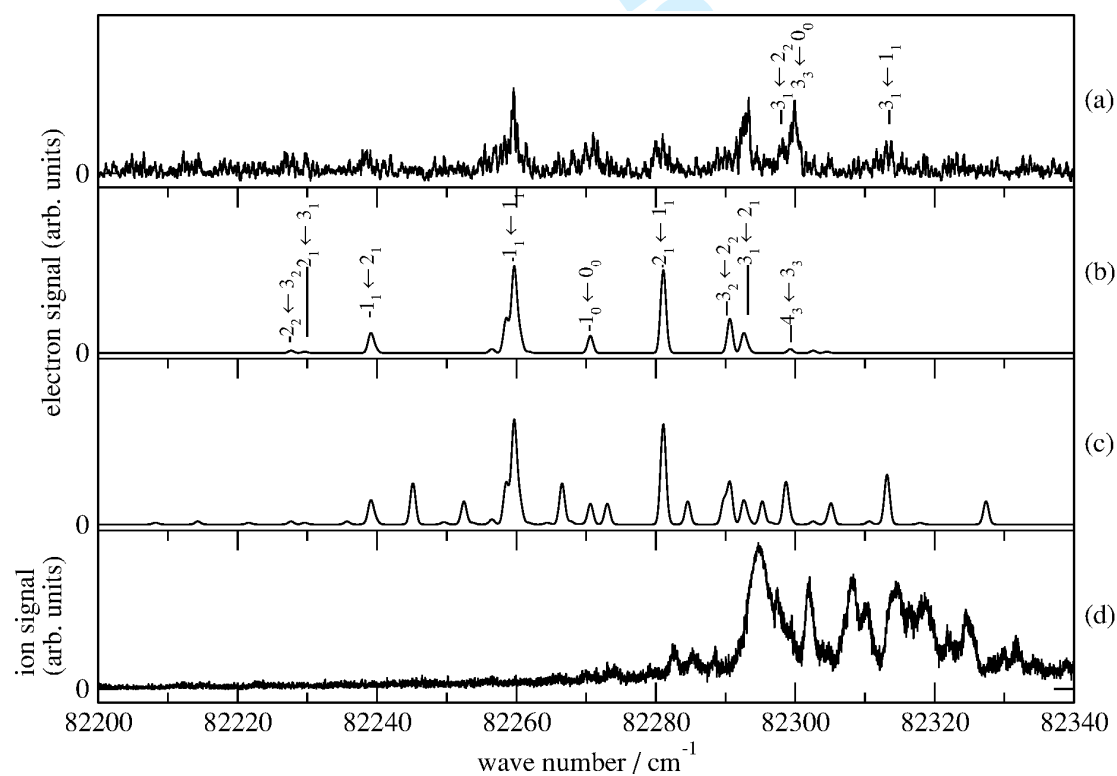


**Figure 1:** (a) PFI-ZEKE photoelectron spectrum of the  $\tilde{X}^+ \ ^2A_2'' (v_2^+ = 0) \leftarrow \tilde{X} \ ^1A_1'$  transition of ND<sub>3</sub>. The lines are assigned using the notation  $N^+_{K^+} \leftarrow N''_{K''}$ . (b) Simulation of the PFI-ZEKE photoelectron spectrum using the orbital ionization model (Eq. 8). (c) Simulation based on a less restrictive photoionization model. (d) Experimental photoionization spectrum of ND<sub>3</sub>.

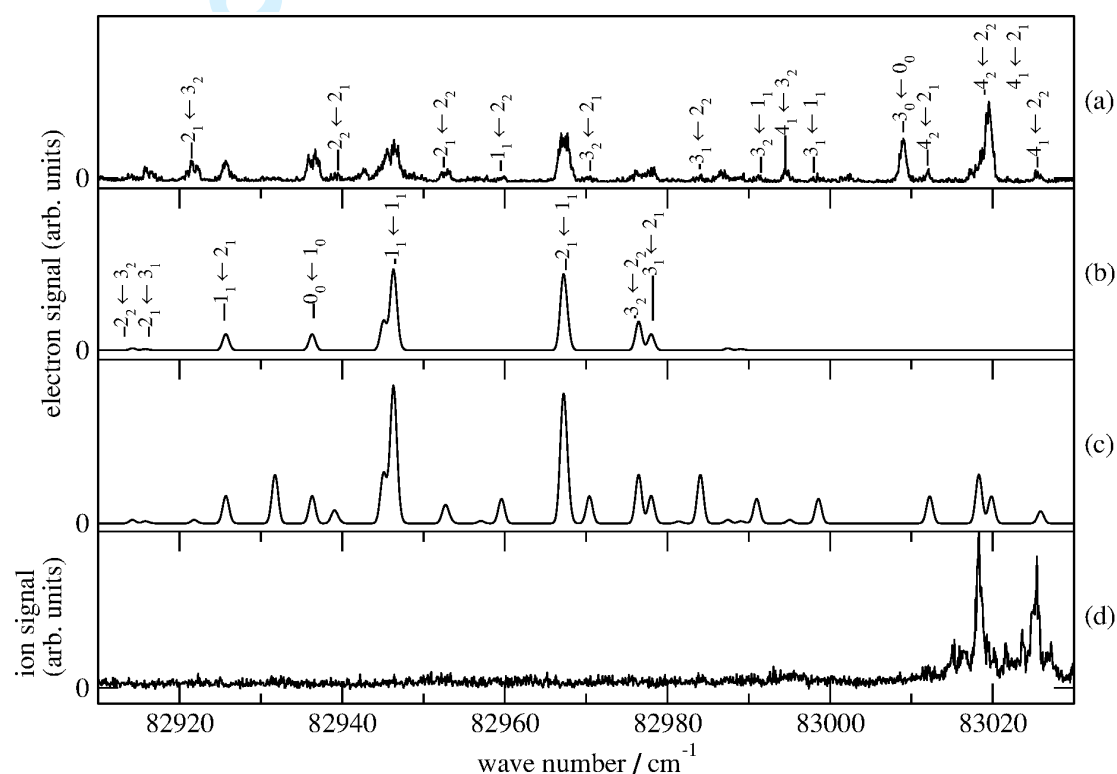


**Figure 2** (a) PFI-ZEKE photoelectron spectrum of the  $\tilde{X}^+ \ ^2A_2'' (v_2^+ = 1) \leftarrow \tilde{X} \ ^1A_1'$  transition of ND<sub>3</sub>. The lines are assigned using the notation  $N^+_{K^+} \leftarrow N''_{K''}$ . (b) Simulation of the PFI-ZEKE photoelectron spectrum using the orbital ionization

1  
2 model (Eq. 8). (c) Simulation based on a less restrictive photoionization model. (d)

3  
4 Experimental photoionization spectrum of ND<sub>3</sub>.  
5  
6  
7  
8  
9  
10  
11  
12  
13  
14  
15  
16  
17  
18  
19  
20  
21  
22  
23  
24  
25  
26  
27  
28  
29  
30  
31  
32  
33  
34  
35  
36  
37  
38  
39  
40  
41  
42  
43  
44  
45  
46  
47  
48  
49  
50  
51  
52  
53  
54  
55  
56  
57  
58  
59  
60

For Peer Review Only

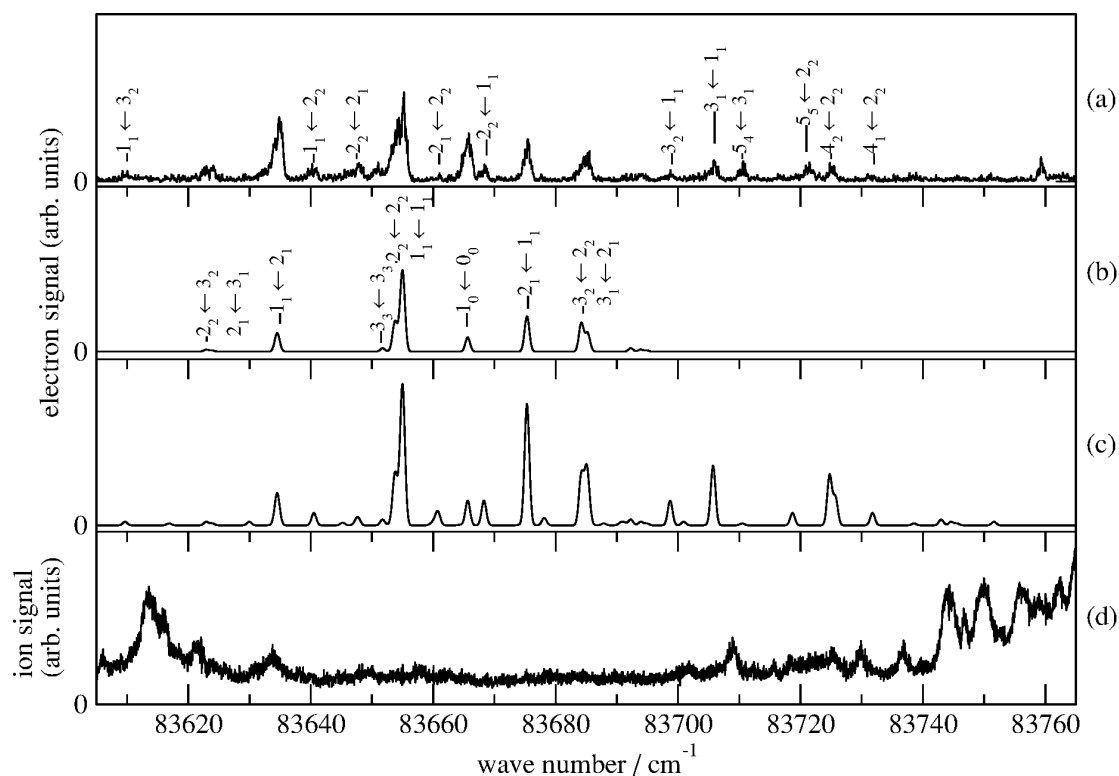


**Figure 3:** (a) PFI-ZEKE photoelectron spectrum of the  $\tilde{X}^+ \ ^2A_2'' (v_2^+ = 2) \leftarrow \tilde{X} \ ^1A_1'$

transition of  $\text{ND}_3$ . The lines are assigned using the notation  $N^+_{K^+} \leftarrow N''_{K''}$ . (b)

Simulation of the PFI-ZEKE photoelectron spectrum using the orbital ionization

model (Eq. 8). (c) Simulation based on a less restrictive photoionization model. (d)

Experimental photoionization spectrum of  $\text{ND}_3$ .

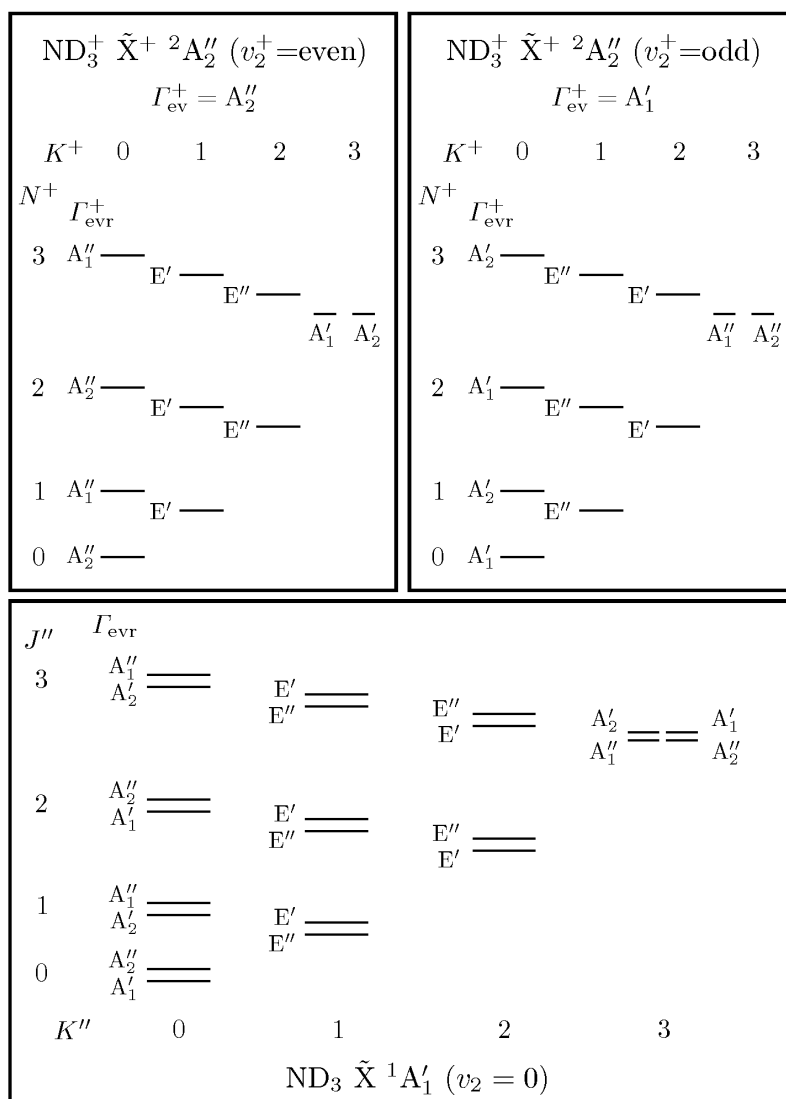


**Figure 4:** Energy level diagram showing schematically the rotational levels of the lowest vibrational level of the  $\tilde{X} ({}^1A_1')$  ground state of  $\text{ND}_3$  (bottom panel) and of out-of-plane bending levels of the  $\tilde{X}^+ ({}^2A_2'')$  ground state of  $\text{ND}_3^+$ , with even values of  $v_2^+$  (top left panel) and odd values of  $v_2^+$  (top right panel). The rovibronic symmetry labels of all levels in the  $D_{3h}(\text{M})$  molecular symmetry group is indicated next to the levels.

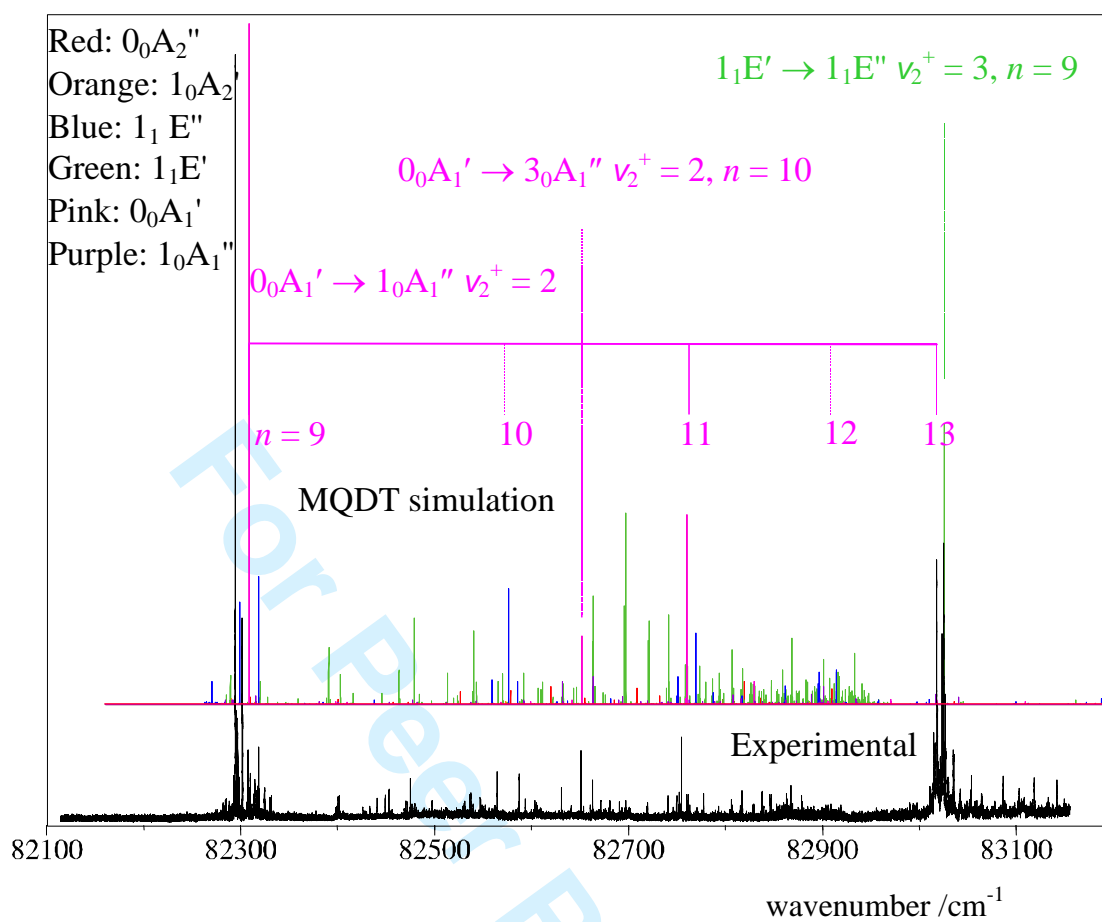


**Figure 5:** Comparison of the photoionization spectrum of  $\text{ND}_3$  (bottom trace, from Ref. [2]) and the MQDT simulation (top trace) calculated using quantum defects from reference [16]: the separate contributions from each initial rotational state are colour coded.

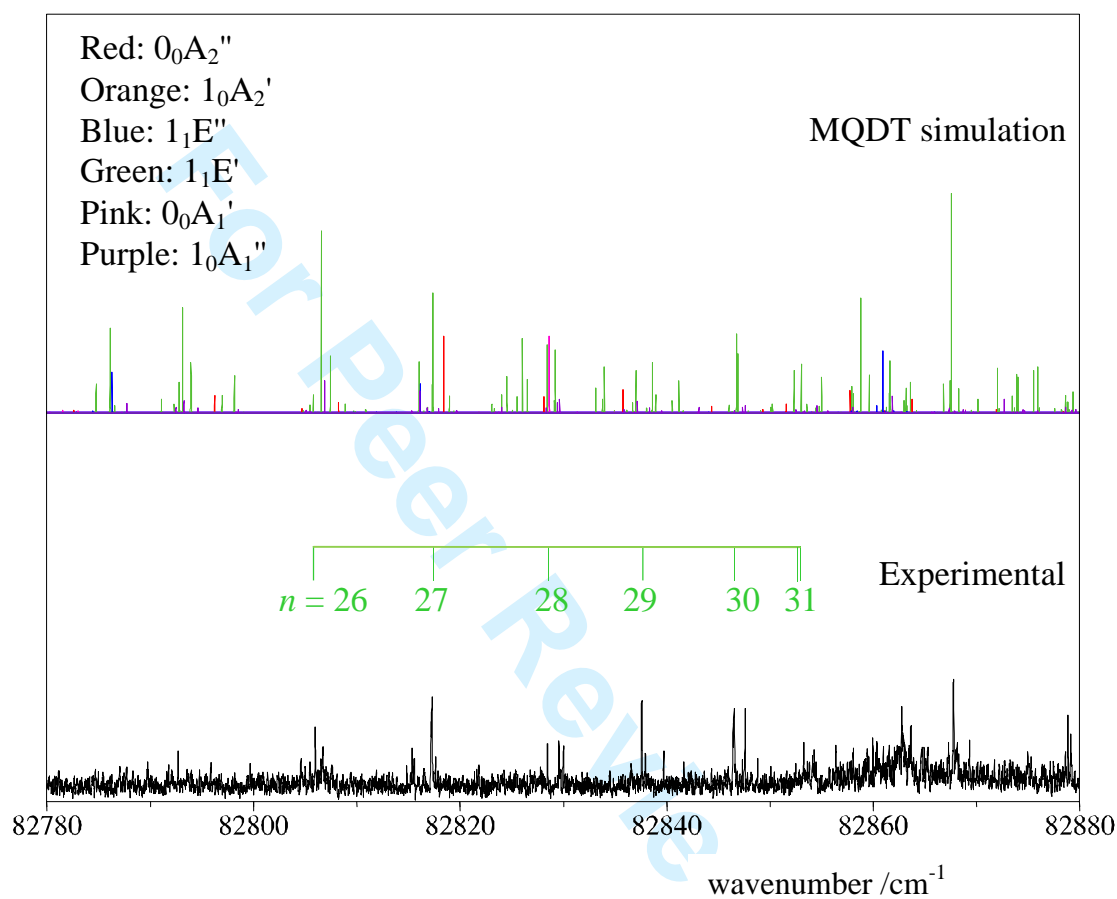


**Figure 6:** Expanded view of the MQDT simulation (top trace) of the  $\text{ND}_3$  photoionization spectrum (bottom trace, ref [2]). The simulated spectrum was computed using quantum defects from reference [16]: the  $v_2^+ = 1$  region is dominated by a series of transitions originating from the  $1_1 E'$  ground state level converging to the  $v^+ = 1$ ,  $1_1 E' \leftarrow 2_1 E''$  rovibronic threshold.

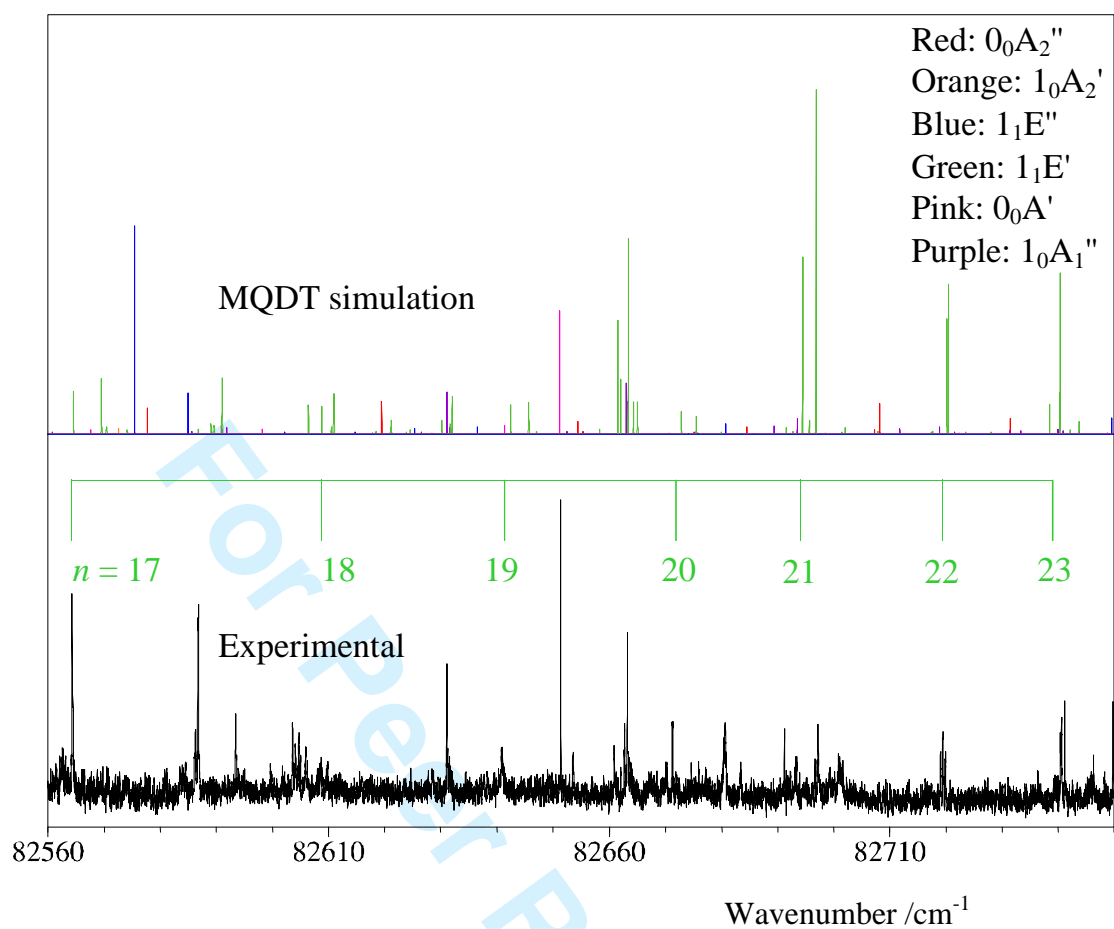


**Figure 7:** Expanded view of the MQDT simulation (top trace) of the  $\text{ND}_3$  photoionization spectrum (bottom trace, ref [2]). The simulated spectrum was computed using quantum defects from reference [16]:  $v_2^+ = 1$  region showing a part of the Rydberg series converging to the  $1_1E' \leftarrow 1_1E''$  rovibronic threshold.

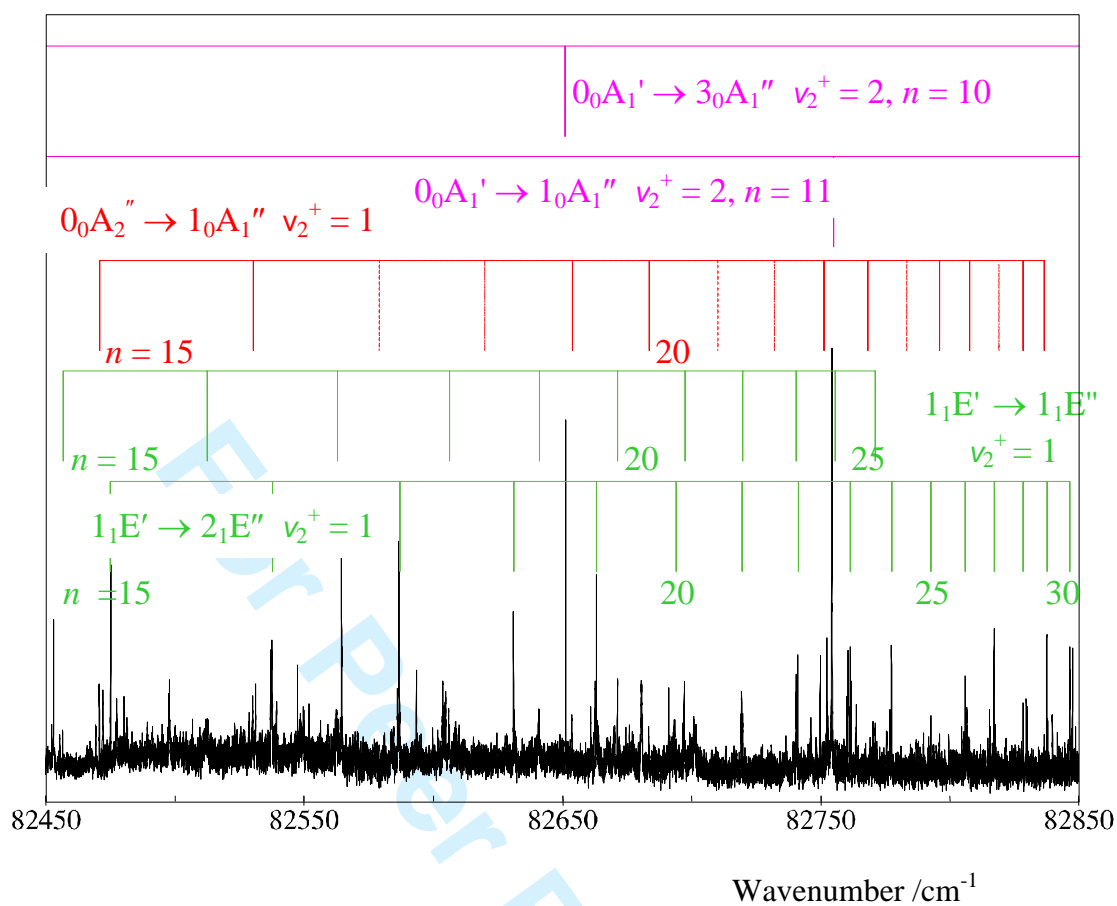


**Figure 8:** Example of series assignments based on the MQDT calculations in a selected region of the high resolution photoionization spectrum of  $\text{ND}_3$  (reported in Ref [2].)

Band	$2_0^0$	$2_0^1$	$2_0^2$
Discrimination pulsed field / $\text{Vcm}^{-1}$	+0.133	+0.133	+0.066
Extraction pulsed field/ $\text{Vcm}^{-1}$	-0.266	+0.133	-0.266
Induced shift of ionization threshold / $\text{cm}^{-1}$	-1.7	-1.5	-1.45

**Table 1:** Two-pulse sequences used to record the PFI-ZEKE photoelectron spectra of  $\text{ND}_3$ . The shifts of the ionization thresholds were estimated as described in reference [20].

$\tilde{\nu}_{\text{exp}} / \text{cm}^{-1}$	$\tilde{\nu}_{\text{exp}} - \tilde{\nu}_{\text{calc}} / \text{cm}^{-1}$	Assignment $N^+_{K^+} \leftarrow N''_{K''}$
82227.7	-0.05	$2_2 \leftarrow 3_2$
82229.7	0.10	$2_1 \leftarrow 3_1$
82239.0	-0.10	$1_1 \leftarrow 2_1$
82259.6	-0.05	$1_1 \leftarrow 1_1$
82270.4	-0.15	$1_0 \leftarrow 0_0$
82281.0	-0.05	$2_1 \leftarrow 1_1$
82290.5	-0.1	$3_2 \leftarrow 2_2$
82292.8	0.15	$3_1 \leftarrow 2_1$
82298.5	-0.1	$3_1 \leftarrow 2_2$
82300.0	-0.1	$3_3 \leftarrow 0_0$
82313.1	-0.05	$3_1 \leftarrow 1_1$

**Table 2:** Assignment of rotational lines (in the notation  $N^+_{K^+} \leftarrow N''_{K''}$ ) of the  $v_2^+ = 0$  band of the PFI-ZEKE photoelectron spectrum of  $\text{ND}_3$ . The reported line positions in the first column have not been corrected for the shift due to the pulsed field ionization. The field-free thresholds can be obtained by adding  $1.7 \text{ cm}^{-1}$  to each of the numbers in column 1 (using the data presented in Table 1.) The calculated wavenumbers  $\tilde{\nu}_{\text{calc}}$  are obtained from Eqs. (1) and (2) using the best fit rotational constants, vibrational intervals and the ionization energy given in Table 5.

$\tilde{\nu}_{\text{exp}} / \text{cm}^{-1}$	$\tilde{\nu}_{\text{exp}} - \tilde{\nu}_{\text{calc}} / \text{cm}^{-1}$	Assignment
		$N^+_{K^+} \leftarrow N''_{K''}$
82915.8	0.05	$2_1 \leftarrow 3_1$
82921.8	0.05	$2_1 \leftarrow 3_2$
82925.6	-0.1	$1_1 \leftarrow 2_1$
82936.4	-0.1	$0_0 \leftarrow 1_0$
82939.1	-0.15	$2_2 \leftarrow 2_1$
82946.2	-0.05	$1_1 \leftarrow 1_1$
82952.7	0.05	$2_1 \leftarrow 2_2$
82967.2	0.1	$2_1 \leftarrow 1_1$
82970.4	-0.05	$3_2 \leftarrow 2_1$
82976.2	-0.2	$3_2 \leftarrow 2_2$
82978.0	0.05	$3_1 \leftarrow 2_1$
82984.1	0.05	$3_1 \leftarrow 2_2$
82991.1	-0.1	$3_2 \leftarrow 1_1$
82994.8	-0.2	$4_1 \leftarrow 3_2$
82998.6	0.05	$3_1 \leftarrow 1_1$
83009.1	-0.2	$3_0 \leftarrow 0_0$
83012.1	-0.1	$4_2 \leftarrow 2_1$
83018.4	0.1	$4_2 \leftarrow 2_2$
83019.6	-0.2	$4_1 \leftarrow 2_1$
83025.7	-0.1	$4_1 \leftarrow 2_2$

**Table 3:** Assignment of rotational lines (in the notation  $N^+_{K^+} \leftarrow N''_{K''}$ ) of the  $v_2^+ = 1$  band of the PFI-ZEKE photoelectron spectrum of  $\text{ND}_3$ . The reported line positions in the first column have not been corrected for the shift due to the pulsed field ionization. The field-free thresholds can be obtained by adding  $1.5 \text{ cm}^{-1}$  to each of the numbers in column 1 (using the data presented in Table 1.) The calculated wavenumbers  $\tilde{\nu}_{\text{calc}}$  are obtained from Eqs. (1) and (2) using the best fit rotational constants, vibrational intervals and the ionization energy given in Table 5.

$\tilde{\nu}_{\text{exp}} / \text{cm}^{-1}$	$\tilde{\nu}_{\text{exp}} - \tilde{\nu}_{\text{calc}} / \text{cm}^{-1}$	Assignment $N^+_{K^+} \leftarrow N''_{K''}$
83 609.7	0.05	$1_1 \leftarrow 3_2$
83 622.9	-0.05	$2_2 \leftarrow 3_2$
83 624.0	0.1	$2_1 \leftarrow 3_1$
83 634.2	-0.1	$1_1 \leftarrow 2_1$
83 640.3	-0.15	$1_1 \leftarrow 2_2$
83 647.8	0.1	$2_2 \leftarrow 2_1$
83 651.6	-0.1	$3_3 \leftarrow 3_3$
83 653.9	0.15	$2_2 \leftarrow 2_2$
83 655.1	0.1	$1_1 \leftarrow 1_1$
83 660.9	0.1	$2_1 \leftarrow 2_2$
83 665.7	0.1	$1_0 \leftarrow 0_0$
83 668.4	0.1	$2_2 \leftarrow 1_1$
83 675.4	0.1	$2_1 \leftarrow 1_1$
83 685.0	0.1	$3_1 \leftarrow 2_1$
83 698.8	0.05	$3_2 \leftarrow 1_1$
83 705.8	0.1	$3_1 \leftarrow 1_1$
83 710.5	0.05	$5_4 \leftarrow 3_1$
83 721.1	0.1	$5_5 \leftarrow 2_2$
83 725.0	0.15	$4_2 \leftarrow 2_2$
83 731.6	-0.15	$4_1 \leftarrow 2_2$

**Table 4:** Assignment of rotational lines (in the notation  $N^+_{K^+} \leftarrow N''_{K''}$ ) of the  $v_2^+ = 2$  band of the PFI-ZEKE photoelectron spectrum of  $\text{ND}_3$ . The reported line positions in the first column have not been corrected for the shift due to the pulsed field ionization. The field-free thresholds can be obtained by adding  $1.45 \text{ cm}^{-1}$  to each of the numbers in column 1 (using the data presented in Table 1.) The calculated wavenumbers  $\tilde{\nu}_{\text{calc}}$  are obtained from Eqs. (1) and (2) using the best fit rotational constants, vibrational intervals and the ionization energy given in Table 5.

Parameter	$v_2^+ = 0$	$v_2^+ = 1$	$v_2^+ = 2$
Vibrational term value ( $\text{cm}^{-1}$ )	Expt	0	686.5(20)
	Literature	0	686 <sup>(a)</sup> 683.3 <sup>(b)</sup>
Rotational constant $B^+$ ( $\text{cm}^{-1}$ )	Expt	5.350 (20)	5.230 (20)
	Literature	5.347 <sup>(a)</sup>	5.214 <sup>(a)</sup>
	REMPI	5.361 (1)	5.232 (1)
Rotational constant $C^+$ ( $\text{cm}^{-1}$ )	Expt	2.675 (50)	2.700 (50)
	Literature	2.6238 <sup>(c)</sup>	2.6538 <sup>(d)</sup>
	REMPI	2.626 (1)	2.646 (1)
Adiabatic ionization energy ( $hc.\text{cm}^{-1}$ )	Expt	82261.7 (15)	82948.2(15)
	Literature	82280 (40) <sup>(e)</sup>	83656.9(15)

**Table 5:** Spectroscopic parameters of  $\text{ND}_3/\text{ND}_3^+$ . Parameters labelled ‘Expt’ are from the present work, while those labelled ‘REMPI’ are from the 2 + 1 REMPI studies of the  $\tilde{C}'$  state of  $\text{ND}_3$  [26]. Other values are determined as follows:

<sup>(a)</sup> Theoretically determined from an adjusted *ab-initio* potential surface [25]. <sup>(b)</sup>

Infrared spectrum of  $\text{ND}_3^+$  recorded in solid neon [31]. <sup>(c)</sup> Calculated using the

equation  $C_{0(\text{ND}_3)} \approx \frac{1}{2} C_{0(\text{NH}_3)}$ . <sup>(d)</sup> Calculated using the  $C_2 - C_1$  and  $C_1 - C_0$  values in

reference [25]. <sup>(e)</sup> Experimental measurement from REMPI studies in ref [8].

$\ell\lambda$	$s\sigma$	$p\sigma$	$p\pi$	$d\sigma$	$d\pi$	$d\delta$
$\mu_{\ell\lambda}$	0.966	0.366	0.577	-0.084	-0.103	0.133
$\ell\lambda - \ell'\lambda'$	$s\sigma - d\sigma$	$p\pi - d\delta$	$s\sigma - p\sigma$	$p\sigma - d\sigma$	$p\pi - d\pi$	$d\pi - d\delta$
$\mu_{\ell\lambda, \ell'\lambda'}$	0.095	-0.075				
$\mu_{\ell\lambda, \nu, \ell'\lambda', \nu+1}$			-0.020	0.024	-0.018	0.015

**Table 6:** Diagonal and off-diagonal quantum elements of the electronic quantum defect matrix used in the MQDT simulations (from ref [16]). The final row lists the vibrationally integrated off-diagonal elements as given in Eq (17).

Molecule			Ion			
$J''$	$K''$	Symmetry	$v_2^+$	$N^+$	$K^+$	Symmetry
1	1	$E'$	1	1	1	$E''$
1	1	$E'$	1	2	1	$E''$
0	0	$A_2''$	1	1	0	$A_2'$
0	0	$A_1'$	2	1	0	$A_1''$
0	0	$A_1'$	2	3	0	$A_1''$
1	1	$E'$	3	1	1	$E''$

**Table 7** Summary of series or parts of series identified in the high-resolution photoionization spectrum of  $\text{ND}_3$ .

Isotopomer	Ionization Energy/cm <sup>-1</sup> ( $\nu_2^+ = 0$ )	Ionization Energy/cm <sup>-1</sup> ( $\nu_2^+ = 1$ )	Ionization Energy/cm <sup>-1</sup> ( $\nu_2^+ = 2$ )	Ionization Energy/cm <sup>-1</sup> ( $\nu_2^+ = 3$ )
<b>NH<sub>3</sub></b>	82158.751(16)			
<b>NH<sub>2</sub>D</b>		83027(3)	83790 (5)	84792.9 (6)
<b>ND<sub>2</sub>H</b>		82990(3)		84595.9 (8)
<b>ND<sub>3</sub></b>	82261.7(15)	82948.2(15)	83656.9 (15)	

**Table 8** Ionization energies (band origins for transitions to specific vibrational thresholds) derived from the present work and references [2,16,17] for NH<sub>3</sub>, NH<sub>2</sub>D, NHD<sub>2</sub> and ND<sub>3</sub>

1  
2  
3  
4  
5  
6  
7  
8  
9  
10  
11  
12  
13  
14  
15  
16  
17  
18  
19  
20  
21  
22  
23  
24  
25  
26  
27  
28  
29  
30  
31  
32  
33  
34  
35  
36  
37  
38  
39  
40  
41  
42  
43  
44  
45  
46  
47  
48  
49  
50  
51  
52  
53  
54  
55  
56  
57  
58  
59  
60

For Peer Review Only